Journal of Power Sources 196 (2011) 6493–6497

Contents lists available at ScienceDirect

Journal of Power Sources

journal homepage: www.elsevier.com/locate/jpowsour

Short communication

Nano-sized $LiMn_2O_4$ spinel cathode materials exhibiting high rate discharge capability for lithium-ion batteries

Yingchao Chen*, Kai Xie, Yi Pan, Chunman Zheng

College of Aerospace and Materials Engineering, National University of Defense Technology, Changsha, 410073, PR China

ARTICLE INFO

Article history:
Received 13 January 2011
Received in revised form 1 March 2011
Accepted 28 March 2011
Available online 4 April 2011

Keywords:
Lithium-ion batteries
Lithium manganese oxide
High rate

ABSTRACT

Nano-sized $LiMn_2O_4$ spinel with well crystallized homogeneous particles (60 nm) is synthesized by a resorcinol–formaldehyde route. Micro-sized $LiMn_2O_4$ spinel with micrometric particles (1 μm) is prepared by a conventional solid-state reaction. These two samples are characterized by XRD, SEM, TEM, BET, and electrochemical methods. At current rate of 0.2*C* (1*C* = 148 mA g^{-1}), a discharge capacity of 136 mAh g^{-1} is obtained on the nano-sized $LiMn_2O_4$, which is higher than that of micro-sized one (103 mAh g^{-1}). Furthermore, compared to the micro-sized sample, nano-sized $LiMn_2O_4$ shows much better rate capability, i.e. a capacity of 85 mAh g^{-1}, 63% of that at 0.2*C*, is realized at 60*C*. The excellent high rate performance of nano-sized $LiMn_2O_4$ spinel may be attributed to its impurity-free nano-sized particles, higher surface area and well crystalline. The outstanding electrochemical performances demonstrate that the nano-sized $LiMn_2O_4$ spinel will be the promising cathode materials for high power lithium-ion batteries used in hybrid and electric vehicles.

Crown Copyright © 2011 Published by Elsevier B.V. All rights reserved.

1. Introduction

In recent years, high power lithium-ion batteries are increasingly required due to high power applications in hybrid electric vehicles, portable power tools and medical equipments [1–3]. Cathode materials are the key component of lithium-ion batteries that directly determines the power density. An effective route to increase power density of the cathode materials is to develop nano-sized particles [4]. Their reduced dimensions increase significantly the rate of Li^+ insertion/removal, because of the short distances for Li^+ transport within the particles and the high interfacial area between active material and electrolyte [5].

Lithium manganese oxide, $LiMn_2O_4$, with the cubic spinel structure, is a promising alternative cathode material for lithium-ion batteries by virtue of the advantages such as good rate capacity, high potential, high abundance of Mn in the earth, low cost, low toxicity and good safety [6,7]. So it is significant to synthesize and investigate the nano-sized $LiMn_2O_4$ spinel with high rate capability. In general, $LiMn_2O_4$ spinel has been synthesized by conventional solid-state reactions that involve the mechanical mixing of lithium and manganese salts followed by high temperature calcination and extended grinding. This method has many disadvantages: impurity phases, inhomogeneity, irregular morphology, large particle size and broad particle size distribution [8–10]. In order to overcome these disadvantages, several low temperature techniques have been developed to prepare the desired nano-sized $LiMn_2O_4$ spinel, such as sol–gel method [11,12], Pechini process [13], combustion process [14], chemical precipitation [15], explosive process [16] and hydrothermal method [17].

In the present work, we reported the synthesis and electrochemical performances of a nano-sized $LiMn_2O_4$ spinel prepared by a novel resorcinol–formaldehyde route. For comparison, micro-sized $LiMn_2O_4$ spinel was also synthesized by a conventional solid-state reaction and tested electrochemically. To understand the improved rate capability of the nano-sized $LiMn_2O_4$, structure and morphology were also investigated.

2. Experimental

2.1. Sample preparation and characterization

Nano-sized $LiMn_2O_4$ spinel was synthesized by a novel resorcinol–formaldehyde (RF) route. 0.08 mol $LiCH_3COO{\cdot}2H_2O$, 0.16 mol $Mn(CH_3COO)_2{\cdot}4H_2O$ (99% purity, Alfa Aesar) were dissolved in 200 ml of ethanol containing 0.4 mol of resorcinol (99% purity, Alfa Aesar) and 0.6 mol of formaldehyde (36.7% in water, methanol stabilized, Alfa Aesar) and mixed thoroughly, then the solution was maintained at 60 °C until a pink transparent gel was obtained. The resultant gel was pyrolyzed at 360 °C for 10 h in air to remove the organic contents. This heat pyrolyzed precursor (RF-360) was ground to a fine powder and calcined at 650 °C in air for 10 h to obtain the final spinel product (RF-650).

* Corresponding author. Tel.: +86 731 84573150; fax: +86 731 84573150.
E-mail addresses: cycdh2007@yahoo.cn, cycdh2007@163.com (Y.C. Chen).

0378-7753/$ – see front matter. Crown Copyright © 2011 Published by Elsevier B.V. All rights reserved.
doi:10.1016/j.jpowsour.2011.03.081

Micro-sized $LiMn_2O_4$ spinel was prepared using a conventional solid-state reaction (SSR) methods from a stoichiometric mixture of $LiCH_3COO{\cdot}2H_2O$ and $Mn(CH_3COO)_2{\cdot}4H_2O$ (99% purity, Alfa Aesar). The well-milled solid mixtures were preheated at 360 °C for 10 h in air and the obtained powders were well ground at room temperature. The well-ground powders (SSR-360) were calcined again at 650 °C for 10 h in air and then ground after being cooled to room temperature. Thus the final product (SSR-650) was obtained.

Thermogravimetry (TG) and differential thermal analysis (DTA) were conducted in air from room temperature to 900 °C on a TA SDT-Q600 thermal analysis system at a scan rate of 10 °C min^{-1}. The phase purity, crystal structure, and lattice parameters of the samples were characterized by a Rigaku TTR-3 Powder X-ray diffraction (XRD), using Cu Kα radiation, in the range of 10–70° (2θ). Surface area measurements of the powders were conducted using BET method by a NOVA-1000 instrument and nitrogen gas. Morphological studies were carried out using a Hitachi S-4800 field emission scanning electron microscopy (FESEM) and a FEI F20 transmission electron microscopy (TEM).

2.2. Electrochemical measurements

The electrode was prepared by following processes. First, the slurry was formed by mixing 80 wt% $LiMn_2O_4$ spinel, 10 wt% acetylene black and 10 wt% PVDF binder (dissolved in NMP). The mixed slurry was coated onto an aluminum current collector with typical active material loading of about 3 mg cm^{-2}. Then the electrodes were dried under vacuum at 110 °C for 12 h and then punched out and weighed.

The cells were assembled in an argon-filled glovebox (Mikrouna, China). A Li metal foil (99.9% purity, 200 μm thick) was used as the reference electrode and counter electrode, while the positive was used as the working electrode. The 1.0 M commercial $LiPF_6$ in EC:DEC (1:1 in volume) was used as the electrolyte and Celgard 2400 membrane as the separator.

The cyclic voltammograms (CVs) were conducted via a three-electrode system with lithium metal as the counter and reference electrodes. The scan was performed at a sweep rate of 0.1 mV s^{-1} from 3.2 to 4.5 V (vs. Li/Li^+) using an Autolab Pgstat30 electrochemical workstation. Charge–discharge tests were conducted galvanostatically on a LAND CT2001A multi-channel battery tester between 3.0 V and 4.3 V (vs. Li/Li^+) at room temperature.

3. Results and discussion

3.1. Structure and morphology characterization of samples

Fig. 1 shows the TG-DTA curves for the thermal decomposition of the resultant gel at a heating rate of 10 °C min^{-1}. Large weight loss (about 50 wt%) was observed at above 360 °C, corresponding to an obvious exothermal peak in the DTA curve at about 390 °C. The peak can be ascribed to the decomposition of organic contents and the formation of the spinel $LiMn_2O_4$ phase as confirmed by following XRD characterization.

The XRD patterns of the samples are shown in Fig. 2. Fig. 2a shows the XRD of a product (RF-360) obtained by heating the precursor at 360 °C, and the spinel structure was observed although the peaks are relatively broad. This suggests that crystallization of spinel could occur at a low temperature of 360 °C in our system. When the precursor was calcined at a higher temperature of 650 °C, the diffraction peaks become both stronger and narrower (Fig. 2b), corresponding to the improved crystalline and more ordered spinel structure. The observed spinel structure in samples RF-360 and RF-650 belongs to a cubic structure with space group of *Fd3m*, wherein the lithium ions occupy 8a sites, the manganese ions occupy 16d sites and oxygen ions occupy 32e sites [18,19]. The refined lattice parameter of RF-650 are a_0 = 8.2343 Å, is close to the standard data (a_0 = 8.236 Å) given by JCPDS 88-1026.

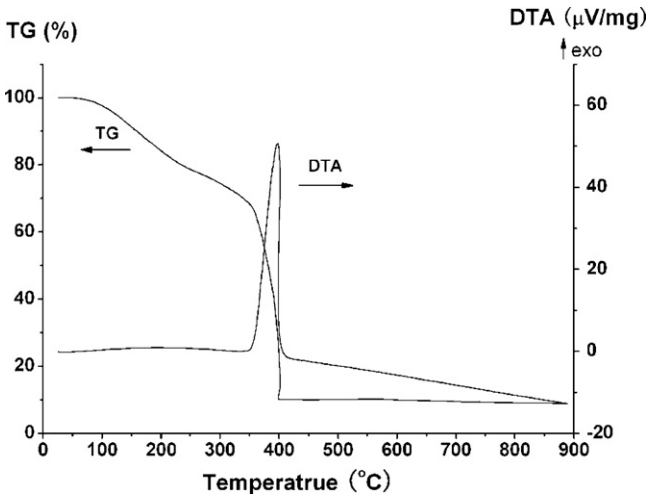

Fig. 1. TG–DTA curves of the resultant gel at a heating rate of 10 °C min^{-1} in air.

While in the case of solid state reaction synthesis, as shown in Fig. 2c, impurity phases of Mn_3O_4 and MnO were detected in the sample preheated at 360 °C (SSR-360). Even for the product synthesized at high temperature of 650 °C (SSR-650), diffractions from impurity of Mn_2O_3 were also observed (Fig. 2d). That may be caused by the inadequate mixing of starting materials in the solid state reaction, which is consistent to the reported results [20].

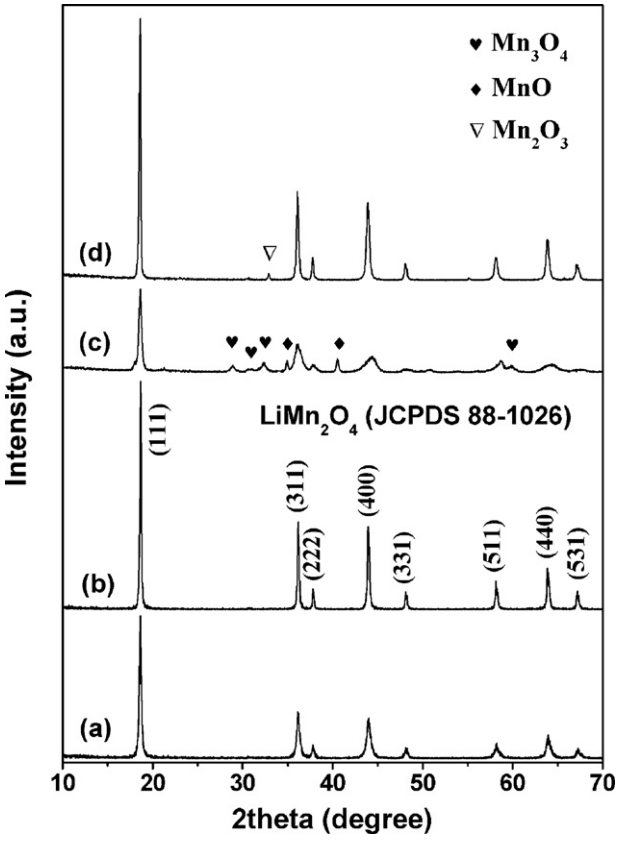

Fig. 2. XRD patterns of the samples: (a) RF-360, (b) RF-650, (c) SSR-360, and (d) SSR-650.

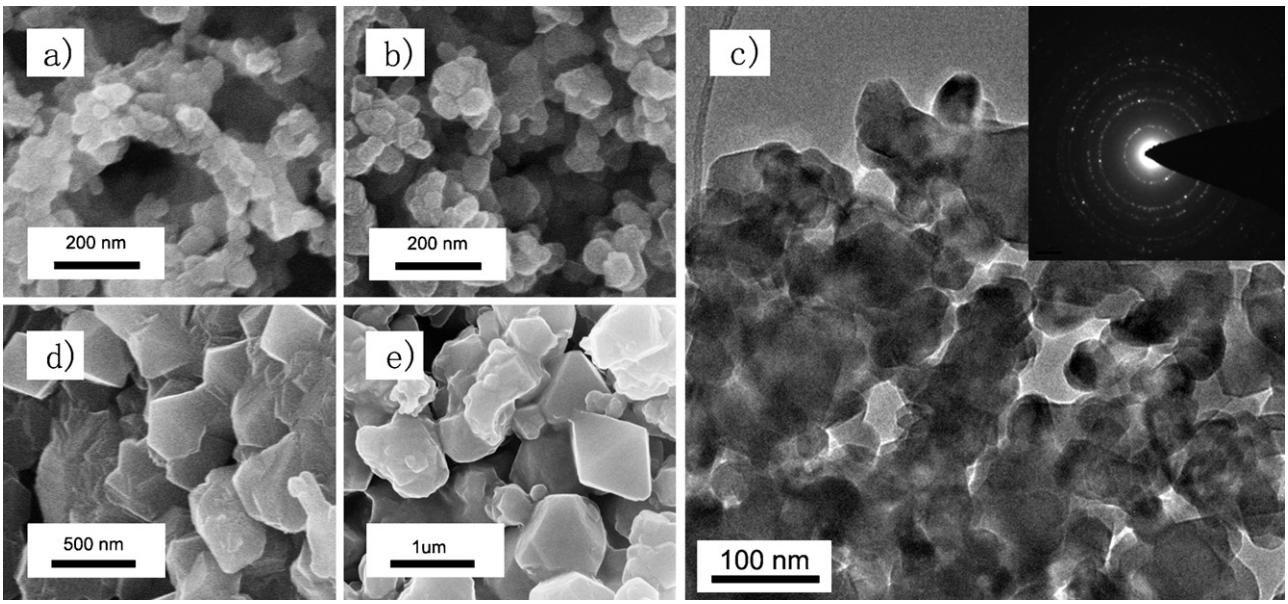

Fig. 3. (a) FESEM image of RF-360, (b) FESEM image of RF-650, (c) TEM image of RF-650, (d) FESEM image of SSR-360, and (e) FESEM image of SSR-650.

Fig. 3 shows the FESEM and TEM images of the samples. It can be seen from Fig. 3a and b that the pyrolyzed precursor RF-360 and final product RF-650 have a porous morphology, composed of interconnected nano-sized particles (50–100 nm). The porous morphology may be attributed to the action of the resorcinol and formaldehyde that form a complex organic network where the metal ions are uniformly distributed in the matrix, and the resultant gel is of atomic scale and homogeneously mixed with each other. Thus, during thermal decomposition process it may be able to prevent phase separation and lead to the formation of homogeneous nano-sized particles. Fig. 3c shows TEM image of the sample RF-650, it can be seen that the average grain size is about 60 nm. The selected area electron diffraction (SAED) pattern corresponding to a group of RF-650 particles is shown in Fig. 3c (inset), the SAED pattern shows the RF-650 particles are crystalline. Fig. 3d and e shows the FESEM images of the preheated sample SSR-360 and the final product SSR-650. It can be seen that the active mass has nearly cubic morphology with a diameter of about 1 μm.

3.2. Electrochemical performance

Fig. 4 shows the initial charge–discharge curves of the sample RF-650 and SSR-650 at 0.2*C* (29.6 mA g^{-1}). Both samples exhibit two plateaus around 3.95 and 4.1 V in the charge–discharge curves. This is due to two-step oxidation/reduction process, which is a characteristic of $LiMn_2O_4$ spinel. The initial charge and discharge specific capacities of the sample RF-650 were 141 and 136 mAh g^{-1} (corresponding to 92% of the theoretical capacity of 148 mAh g^{-1}), respectively, indicating a columbic efficiency of 96.5%. While the initial charge and discharge specific capacities of the sample SSR-650 are only 119 and 103 mAh g^{-1} respectively. Compared to sample RF-650, lower discharge potential was also observed on sample SSR-650. According to the XRD and SEM characterization, it is the observed poor phase purity and the larger size particles on sample SSR-650, that may be responsible for the decreased electrochemical properties.

The rate capabilities of the sample RF-650 and SSR-650 are shown in Fig. 5. The rate capability was expressed as ratios of discharge capacities at various C-rates vs. those obtained at 0.2*C* (Fig. 5a). The discharge curves of the sample RF-650 and SSR-650 at various C-rates are shown in Fig. 5b and c. Much improved rate capability was observed on sample RF-650. For example, the initial discharge capacity of 107 mAh g^{-1}, 79% of that at 0.2*C*, was obtained on the sample RF-650 at 40*C*, while only a 44 mAh g^{-1} could be realized on sample SSR-650 at 10*C*. The excellent rate capability was also proved by comparing the potential drop of those two samples, i.e., much high potential polarization was observed on the sample SSR-650. According to the BET surface measurement, sample SSR-650 has a much higher surface area (12.6 m^2 g^{-1}) than that of SSR-650 (1.67 m^2 g^{-1}). As a result, the sample RF-650 composed of impurity-free nano-sized particles with large interface area can provide more area contacting with electrolyte and short diffusion length for deintercalation/intercalation of lithium ions in charge–discharge processes, attributing to the excellent high rate performance at high current rates [7,21].

To address the excellent rate capability of the nanosized RF-650, the cyclic voltammograms were used to study the oxidation/reduction and/or phase transformation processes in electrode reactions [22–24]. For comparison, CVs have been performed on both the sample RF-650 and SSR-650. Fig. 6 presents the nor-

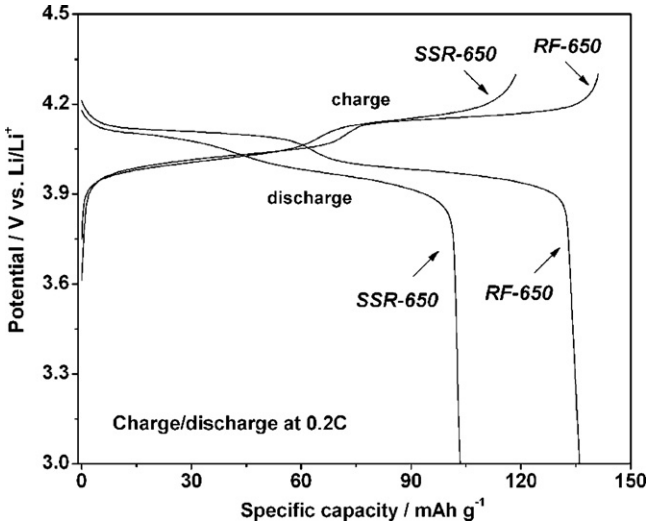

Fig. 4. Initial charge–discharge curves of the sample RF-650 and SSR-650 at 0.2*C* between 3.0 and 4.3 V.

Table 1
Cyclic voltammogram peaks of the sample RF-650 and SSR-650.

Sample	Forward scan (charge process)		Backward scan (discharge process)	
	Peak A1 (V)	Peak A2 (V)	Peak C2 (V)	Peak C1 (V)
Nano-sized RF-650	4.037	4.164	4.073	3.962
Micro-sized SSR-650	4.046 (+0.009)	4.185 (+0.021)	4.059 (−0.014)	3.944 (−0.018)

Values in brackets are difference compared with the sample RF-650.

mal CV scans measured between 3.2 and 4.5 V at a sweep rate of 0.1 mV s^{-1}. The CV curves exhibit two pairs of clearly separated oxidation/reduction peaks. The high potential pair of peaks is attributed to Li^+ insertion/removal from the 8a sites where Li–Li interactions do not occur, corresponding to Li^+ insertion/removal over the x value range of $0 \le x \le 0.5$ in $Li_xMn_2O_4$. The low potential pair of peaks is attributed to Li^+ insertion/removal from the 8a sites but where Li–Li interactions occur, corresponding to Li^+ insertion/removal over the x value range of $0.5 \le x \le 1$ in $Li_xMn_2O_4$ [8]. Compared to sample SSR-650, sample RF-650 shows lower redox potentials in anodic processes while higher redox potentials in cathodic processes. The detailed peak potentials for the sample RF-650 and SSR-650 and their differences are listed in Table 1. This implies higher potential polarization to SSR-650, which agrees well to the results in charge–discharge processes (Fig. 5).

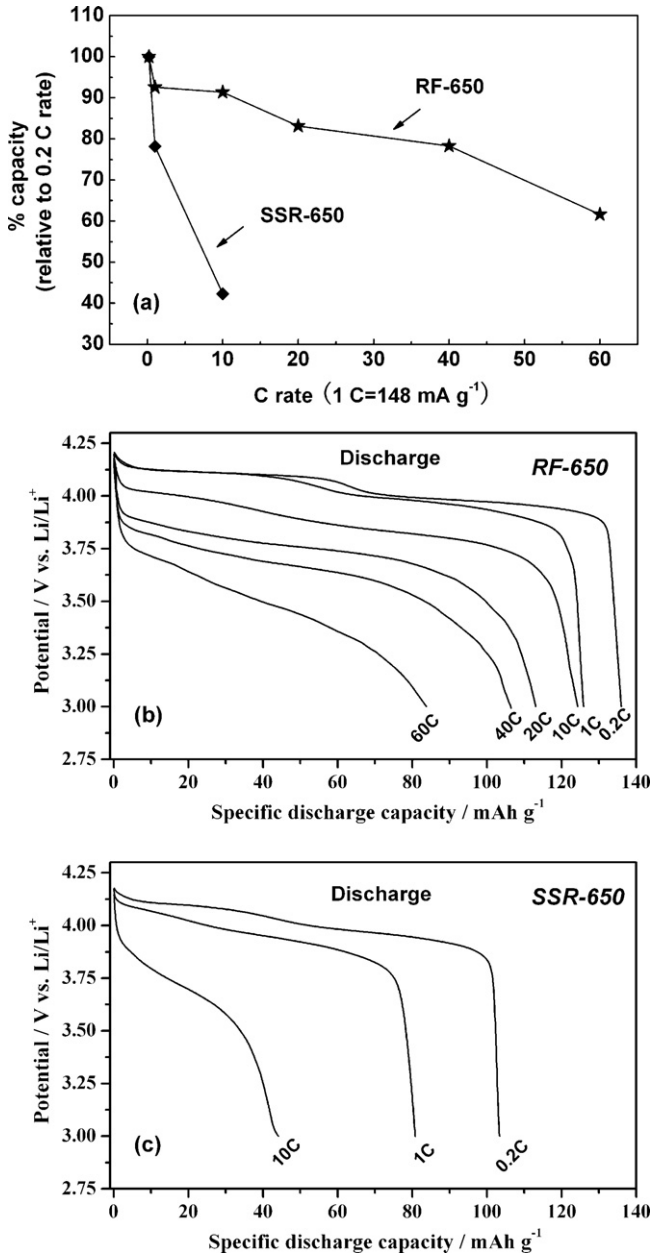

Fig. 5. (a) Rate performances of RF-650 compared with SSR-650. (b) The discharge curves of RF-650 at various C-rates. (c) The discharge curves of SSR-650 at various C-rates.

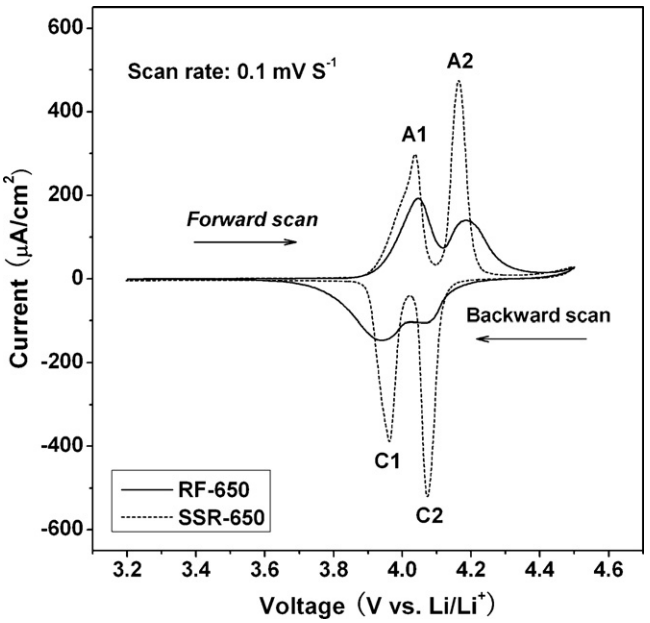

Fig. 6. Cyclic voltammograms of the sample RF-650 and SSR-650.

4. Conclusions

The nano-sized $LiMn_2O_4$ (RF-650) spinel with well crystallized homogeneous particles (60 nm) has been synthesized by a resorcinol–formaldehyde route. Micro-sized $LiMn_2O_4$ spinel (SSR-650) with micrometric particles (1 μm) has been prepared by a conventional solid-state reaction. Electrochemical tests reveal the sample RF-650 exhibits a high initial discharge capacity (136 mAh g^{-1}) at a rate of 0.2*C* (29.6 mA g^{-1}), which is much higher than those of the sample SSR-650 (103 mAh g^{-1} at 0.2*C*). The former with capacity retention of 79% at 60*C* discharge rate, shows much better high rate capability than the latter. The excellent high rate performance of the sample RF-650 may be attributed to its impurity-free nano-sized particles, higher surface area and well crystalline. The outstanding electrochemical performances demonstrate that the nano-sized $LiMn_2O_4$ spinel (RF-650) will be a promising cathode material for high power lithium-ion batteries needed for hybrid and electric vehicles.

References

[1] B. Scrosati, Nature 373 (1995) 557.
[2] M.S. Whittingham, Chem. Rev. 104 (2004) 4271.

[3] B. Kang, G. Ceder, Nature 458 (2009) 190.
[4] C.H. Jiang, E. Hosono, H.S. Zhou, Nanotoday 1 (2006) 28.
[5] P.G. Bruce, B. Scrosati, J.M. Tarascon, Angew. Chem. Int. Ed. 47 (2008) 2930.
[6] M.M. Thackeray, J. Electrochem. Soc. 142 (1995) 2558.
[7] S.H. Ye, J.Y. Lv, X.P. Gao, F. Wu, D.Y. Song, Electrochim. Acta 49 (2004) 1623.
[8] W. Liu, G.C. Farrington, F. Chaput, B. Dunn, J. Electrochem. Soc. 143 (1996) 879.
[9] P. Endres, B. Fuchs, S.K. Sack, K. Brandt, G.F. Becker, H.W. Praas, Solid State Ionics 89 (1996) 221.
[10] J. Guan, M.L. Liu, Solid State Ionics 110 (1998) 21.
[11] J. Pierre, P. Ramos, J. Power Sources 54 (1995) 120.
[12] B.J. Hwang, R. Santhanam, D.G. Liu, J. Power Sources 101 (2001) 86.
[13] S.H. Wu, H.L. Chen, J. Power Sources 119–121 (2003) 134.
[14] C.Z. Lu, G.T. Fey, J. Phys. Chem. Solids 67 (2006) 756.
[15] A.R. Naghash, J.Y. Lee, J. Power Sources 85 (2000) 284.
[16] X.H. Xie, X.J. Li, Z. Zhao, H.B. Wu, Y.D. Qu, W.Y. Huang, Powder Technol. 169 (2006) 143.
[17] H.M. Wu, J.P. Tu, Y.F. Yuan, X.T. Chen, J.Y. Xiang, X.B. Zhao, G.S. Cao, J. Power Sources 161 (2006) 1260.
[18] G.H. Li, H. Ikuta, T. Uchida, M. Wakihara, J. Electrochem. Soc. 143 (1996) 178.
[19] S.T. Myung, H.T. Chung, S. Komaba, N. Kumagai, H.B. Gu, J. Power Sources 90 (2000) 103.
[20] V. Berbenni, A. Marini, J. Anal. Appl. Pyrol. 70 (2003) 437.
[21] Y.L. Zhang, H.C. Shin, J. Dong, M.L. Liu, Solid State Ionics 171 (2004) 25.
[22] N. Ding, J. Xu, Y.X. Yao, G. Wegner, X. Fang, C.H. Chen, I. Lieberwirth, Solid State Ionics 180 (2009) 222.
[23] S.B. Tang, M.O. Lai, L. Lu, Mater. Chem. Phys. 111 (2008) 149.
[24] S.R. Das, S.B. Majumder, R.S. Katiyar, J. Power Sources 139 (2005) 261.